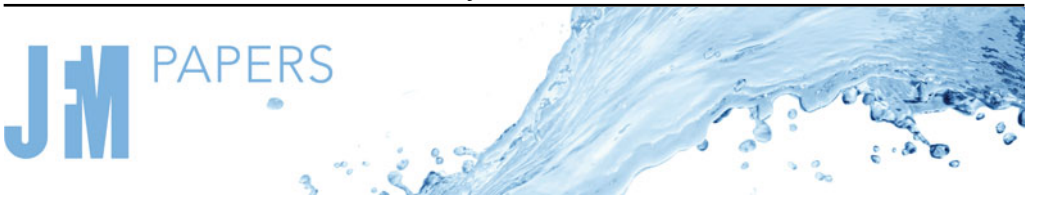
J. Fluid Mech. (2026), *vol.* 1038, A53, doi:10.1017/jfm.2026.11791



Linking flow structures and aerodynamic performance for low-aspect-ratio plates at low Reynolds numbers

Yichen Zhu[1], **Jiaxin Liu**[1], **Jinjun Wang**[1] **and Lihao Feng**[1]

[1]Fluid Mechanics Key Laboratory of Education Ministry, Beijing University of Aeronautics and Astronautics, Beijing 100191, PR China

Corresponding author: Jinjun Wang, jjwang@buaa.edu.cn

(Received 15 November 2025 UTC; revised 30 April 2026 UTC; accepted 6 June 2026 UTC)

This study presents an experimental investigation of the flow over a trapezoidal plate and its wake at a chord-based Reynolds number of 5800. The plate has an aspect ratio of 1.38 and the angle of attack varies from 4° to 10°. Volumetric flow fields are acquired through stereoscopic particle image velocimetry and aerodynamic forces are estimated via the wake-integral approach. A key novel finding is achieved: the swallow-tailed separation bubble, characterised by a distinct concavity, enables the plate to achieve its maximum lift-to-drag ratio. This favourable performance arises from the formation of a counter-rotating vortex pair in the vicinity of the bubble concavity. This vortex pair suppresses the velocity deficit in the wake, thereby contributing to drag reduction. Overall, the swallow-tailed separation bubble structure substantially improves aerodynamic efficiency, highlighting the practical potential of spanwise fluid transport mechanism, discussed previously by Zhu *et al.* (*J. Fluid Mech.*, vol. 965, 2023, p. A12), for developing effective physics-based flow control strategies.

Key words: aerodynamics, wakes, low-Reynolds-number flows

1. Introduction

Motivated by growing application requirements, miniaturisation and lightweight design have become key directions for the future development of low-speed aircraft, including micro air vehicles (MAVs) and unmanned aerial vehicles (UAVs). This trend necessitates a more in-depth understanding of aerodynamics at low Reynolds numbers, typically ranging from 10^3 to 10^5. At these scales, viscous forces become increasingly important compared with inertial forces. As a result, while conventional aerofoils achieve optimal performance at high Reynolds numbers, their aerodynamic efficiency deteriorates significantly in the low-Reynolds-number regime (Mueller 1999; Winslow *et al.* 2018). In contrast, flat plates

© The Author(s), 2026. Published by Cambridge University Press.

https://doi.org/10.1017/jfm.2026.11791 Published online by Cambridge University Press

exhibit superior maximum lift-to-drag ratios in this regime, primarily due to aerodynamic shape modifications induced by laminar separation bubbles. For finite-span wings, wingtip vortices interact with these separation bubbles, thereby exerting a profound influence on overall aerodynamic performance.

The interactions between wingtip vortices and separation bubbles have received considerable attention due to their critical role in aerodynamic performance. Toppings & Yarusevych (2021) experimentally investigated the structure and dynamics of laminar separation bubbles under wingtip effects at a chord-based Reynolds number Re_c of 1.25×10^5. They found that wingtip effects predominantly alter flow characteristics near the wingtip, while the separation bubble retains essentially two-dimensional behaviour in the inboard region. Garmann & Visbal (2017) employed high-fidelity implicit large-eddy simulation to study the dynamics of wingtip vortices on a finite-span NACA0012 wing at $Re_c = 2.0 \times 10^5$. They identified corner vortices forming between the wingtip vortex and the leading-edge separated region. These corner vortices remain stationary over the wing surface and interact with the wake vortices. Furthermore, Zhang *et al.* (2020) and Pandi & Mittal (2023) examined the dynamics of leading-edge vortices (LEVs) on finite-span wings at $Re_c = O(10^2)$. They explored a phenomenon termed vortex dislocation, where vortex shedding near the wingtip becomes desynchronised with the two-dimensional vortical structures present in the inboard region. Subsequently, Ribeiro *et al.* (2023*a*,*b*) investigated the effects of wing taper and sweep on the growth of optimal harmonic perturbations and wake dynamics using triglobal resolvent analysis. Similarly, Navrose *et al.* (2019) conducted an optimal perturbation analysis for the vortex system comprising the wingtip vortex, the flow over the wing surface and the axial vorticity roll-up region. The linear optimal perturbation is located near the wing surface, with its strength decreasing from the wing root towards the tip. The nonlinear evolution of this linear optimal perturbation may constitute the underlying mechanism responsible for wingtip vortex wandering.

In the case of low-aspect-ratio (low-$\mathcal{AR}$) wings, interactions among flow structures become increasingly complex, while aerodynamic forces are very small, posing substantial challenges for experimental investigation. In this context, several notable studies in this field are reviewed here. Okamoto *et al.* (2019) successfully measured aerodynamic forces on low-$\mathcal{AR}$ plate wings at $Re_c = 10^3$–10^4 using a specialised low-pressure wind tunnel. By adjusting air density to reduce the Reynolds number while increasing free stream velocity to maintain sufficient dynamic pressure, they ensured measurable aerodynamic force signals. Dong, Choi & Mao (2020) examined the flow over a thin wing with $\mathcal{AR} = 0.5$, demonstrating that the induced velocity of the tip vortex promotes reattachment of the separated flow and maintains the LEV. Moreover, given that butterflies achieve exceptional flight performance using low-$\mathcal{AR}$ wings at low Reynolds numbers, extensive research has been devoted to uncovering the underlying flow mechanisms through biomimetic wing designs (Hu & Wang 2011; Ortega Ancel *et al.* 2017; Zhu *et al.* 2020). With respect to the pronounced wingtip effects characteristic of low-$\mathcal{AR}$ wings, Zhu *et al.* (2023, 2024, 2025) have conducted a series of studies highlighting the critical role of near-wall spanwise fluid transport. Specifically, the separation bubble develops a swallow-tailed structure due to enhanced entrainment in its rear region, driven by near-wall spanwise fluid transport. Meanwhile, this spanwise fluid transport interacts with downwash, influencing the development of LEVs and associated inter-scale energy transfer. Nevertheless, the implications of these flow dynamics for aerodynamic performance require further systematic investigation.

The objective of the present study is to elucidate the implications of flow physics associated with separation bubble development on aerodynamic characteristics.

https://doi.org/10.1017/jfm.2026.11791 Published online by Cambridge University Press

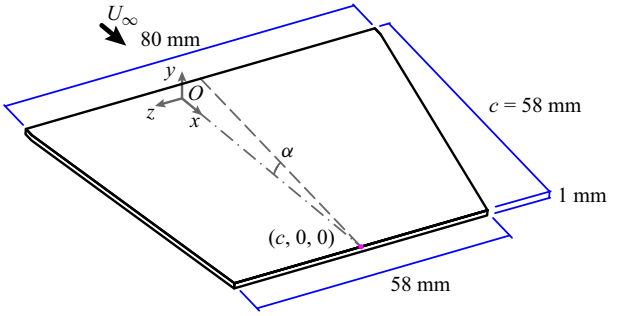


Figure 1. Plate geometry and coordinate system definition.

Specifically, the flow fields over a trapezoidal plate used in our previous studies and the corresponding wakes are measured at various angles of attack. The statistical characteristics of the flow fields are first analysed to explore how separation bubbles affect wake topology. Subsequently, the wake-integral approach is applied for force estimation to establish a direct linkage between flow structures and aerodynamic forces.

2. Experimental methodology

2.1. *Experimental set-up*

The experimental apparatus used in this study is identical to that described by Zhu *et al.* (2023). As shown in figure 1, the plate model is machined from a 1 mm thick aluminium sheet with all edges maintaining a square profile. It has a chord length of $c = 58$mm, a leading-edge length of 80 mm and a trailing-edge length of 58 mm. The aspect ratio is defined as the ratio of maximum span to chord, yielding $\mathcal{AR} = 1.38$. The free stream velocity U_∞ is set to 96 mm s^{-1}, corresponding to a chord-based Reynolds number Re_c of 5800. This value falls within the typical operating regime of flying insects, whose exceptional flight performance is worthy of further exploration. The free stream turbulence intensity remains below 0.8 %. To facilitate data presentation, a Cartesian coordinate system O-xyz is adopted. The origin O is defined such that the coordinates of the trailing-edge point in the midspan plane (magenta point in figure 1) are $(c, 0, 0)$, with the x, y and z axes aligned in the streamwise, vertical and spanwise directions, respectively.

Stereoscopic particle image velocimetry (stereo-PIV) is employed to measure the flow fields over the plate and in its wakes, with the configuration depicted in figure 2. Experiments are conducted in the low-speed recirculation water channel at Beihang University. The water channel is seeded with hollow glass beads of 5–20 μm diameter and illuminated by a dual-head Nd:YAG laser (Beamtech Vlite-500). The laser light sheet remains stationary during experiments and has a thickness of 2 mm. Two charged-coupled device (CCD) cameras (IMPERX ICL-B2520M, 2456 × 2058 pixels) are positioned on opposite sides of the water channel. Equipped with Nikkor 85 mm tilt-shift lenses, these cameras satisfy the Scheimpflug condition. Synchronisation between the cameras and the laser is achieved using a MicroVec Micropulse-725 synchroniser. Particle images are acquired in double-frame mode at a sampling frequency of 3 Hz. Furthermore, the plate model is hung upside down and shifted streamwise through the stationary light sheet via a high-resolution translator. In this manner, a total of 31 closely spaced y–z measurement planes are obtained, spanning from $x/c = -0.03$ to $x/c = 1.52$ with an increment of $\Delta x/c \approx 0.052$ (3 mm). For each plane, 2000 image pairs are recorded.

https://doi.org/10.1017/jfm.2026.11791 Published online by Cambridge University Press

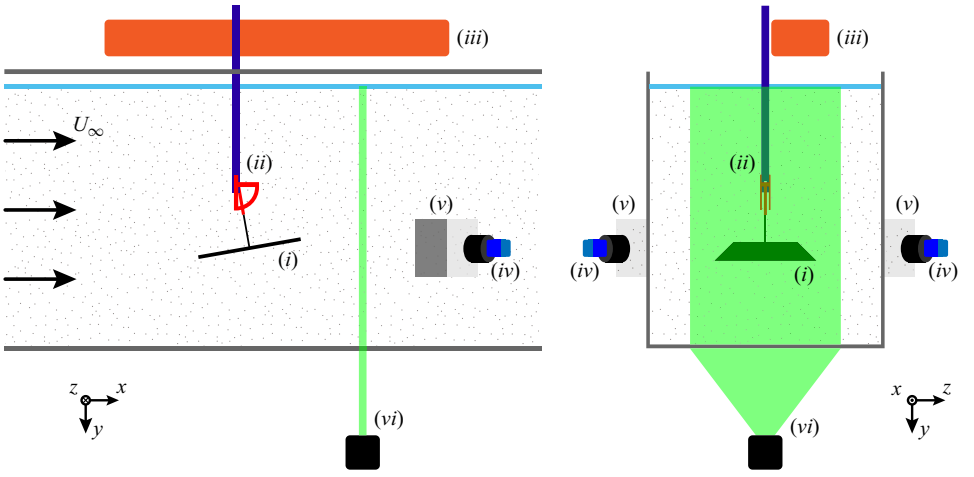


Figure 2. Overview of the stereo-PIV set-up: (*i*) plate model, shown in an enlarged view for clarity; (*ii*) plate support system; (*iii*) high-resolution translator (*iv*) CCD cameras; (*v*) water prisms; (*vi*) laser sheet.

All particle images are pre-processed using a background removal method based on proper orthogonal decomposition (POD) (Sirovich 1987; Mendez *et al.* 2017). A self-calibration method (Wieneke 2005) is applied to correct misalignment between the calibration target and the light sheet. Velocity fields are computed with an in-house stereo-PIV code based on Soloff reconstruction (Soloff, Adrian & Liu 1997) and the optical flow method (Pan *et al.* 2015). The interrogation window size is set to 48×48 pixels with 75 % overlap, yielding a vector spacing of approximately 0.3 mm. Raw velocity data are further validated using robust principal component analysis method (Scherl *et al.* 2020). The uncertainty relative to the free stream velocity is approximately 1.5 % for the velocity fields (Van Doorne & Westerweel 2007). Further experimental details are available from Zhu *et al.* (2023). Distinct from the previous study, the current work focuses on wake characteristics and their correlations with upstream flow structures and aerodynamic forces.

2.2. *Estimating forces based on wake integral*

Given that aerodynamic forces under low Reynolds numbers and other operating conditions are often too small to be measured accurately, several alternative control volume methods have been developed. Among these, the wake-integral approach is widely adopted because it requires data only from a wake plane and provides acceptable accuracy (Roeland & Robert 2016; Wang, He & Liu 2019; Baker *et al.* 2019; Tong, Wang & Yang 2022).

The foundation of the wake-integral approach lies in a global momentum balance over the control volume V_f, which fully encloses the plate model (see figure 3). The volume V_f is bounded by six surfaces Σ, including the inlet surface Σ_∞, the exit wake surface Σ_{wake} and the four peripheral surfaces. The outward-pointing normal vectors of these surfaces are denoted as $\boldsymbol{n}$. The aerodynamic force exerted on the plate can be expressed as

$$\boldsymbol{F} = -\int_{V_f} \frac{\partial\,(\rho \boldsymbol{u})}{\partial t}\,\mathrm{d}V + \int_{\Sigma} (-\rho \boldsymbol{n}\cdot\boldsymbol{u}\boldsymbol{u})\,\mathrm{d}S + \int_{\Sigma} (-p\boldsymbol{n} + \boldsymbol{\tau}:\boldsymbol{n})\,\mathrm{d}S, \tag{2.1}$$

where ρ denotes fluid density, p denotes fluid pressure and $\boldsymbol{\tau}$ denotes viscous stress tensor. The first term on the right-hand side represents unsteady effects. Given that the flow

https://doi.org/10.1017/jfm.2026.11791 Published online by Cambridge University Press

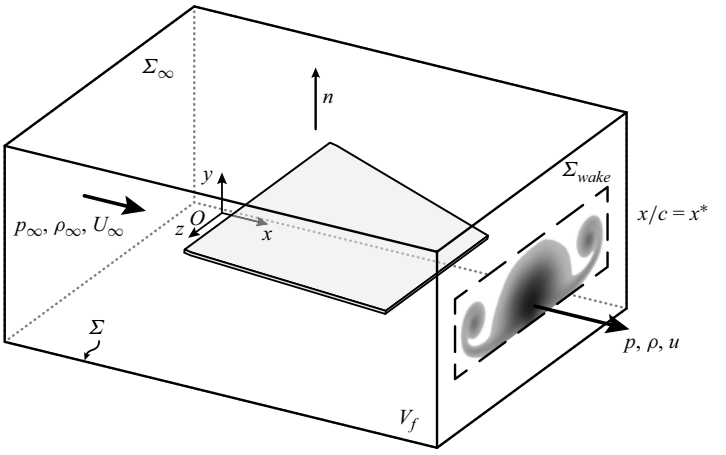


Figure 3. Computational domain V_f for flow past the trapezoidal plate. The wake surface, denoted as Σ_{wake}, is positioned at $x/c = x^*$. The dashed rectangular region on Σ_{wake} is the effective area used for force estimation.

investigated in this study is statistically stationary, this term becomes zero in the evaluation of time-averaged forces and is therefore omitted. Assuming that the four peripheral surfaces are sufficiently far from the plate, the velocity on these surfaces approaches that of the uniform free stream U_∞, allowing the global momentum balance to be simplified to a comparison between Σ_∞ and Σ_{wake}. Consequently, the aerodynamic force acting on the flat plate can be determined solely from the integral over the wake surface Σ_{wake}. The time-averaged lift and drag coefficients are then expressed as

$$\overline{L} = \int_{\Sigma_{wake}} -\rho \overline{uv}\, \mathrm{d}S, \tag{2.2}$$

$$\overline{D} = \int_{\Sigma_{wake}} \rho\left(U_\infty^2 - \overline{u}^2\right)\mathrm{d}S + \int_{\Sigma_{wake}} -\rho\overline{u'u'}\, \mathrm{d}S + \int_{\Sigma_{wake}} (p_\infty - \overline{p})\mathrm{d}S + \int_{\Sigma_{wake}} \overline{\tau}_{xx}\, \mathrm{d}S. \tag{2.3}$$

According to Stokes' theorem, (2.2) can be transformed into

$$\overline{L} = \int_{\Sigma_{wake}} \overline{l}\, \mathrm{d}S = \int_{\Sigma_{wake}} -\rho z \overline{u\omega_x} - \rho z \left(\overline{w}\frac{\partial \overline{u}}{\partial y} - \overline{v}\frac{\partial \overline{u}}{\partial z}\right) - \rho z \left(\frac{\partial \overline{u'w'}}{\partial y} - \frac{\partial \overline{u'v'}}{\partial z}\right) \mathrm{d}S, \tag{2.4}$$

where $\overline{l}$ denote lift element.

As for drag, given that $\overline{\dot{m}} = \int_{\Sigma_{wake}} \rho(\overline{u} - U_\infty)\, \mathrm{d}S$ represents the net mass of fluid generated within the control volume, this term can be reasonably set to zero for incompressible flow. Accordingly, the first term on the right-hand side of (2.3) is transformed to $\int_{\Sigma_{wake}} \rho\overline{u}(\overline{u} - U_\infty)\, \mathrm{d}S$. Moreover, as established in the literature (van Dam 1999), the viscous stress term can be written as

$$\overline{\tau}_{xx} = 2\mu\frac{\partial \overline{u}}{\partial x} - \rho\overline{u'u'}, \tag{2.5}$$

where μ denotes dynamic viscosity. The viscous component $2\mu\partial\overline{u}/\partial x$ is calculated using the in-plane velocity gradients, given that the flow divergence is zero. The second term on the right-hand side of (2.3) is obtained via the pressure reconstruction based on the

https://doi.org/10.1017/jfm.2026.11791 Published online by Cambridge University Press

Poisson equation,

$$\nabla^2 \overline{p} = -\nabla \cdot \left\{ \rho \left((\overline{\boldsymbol{u}} \cdot \nabla)\, \overline{\boldsymbol{u}} + \nabla \overline{\boldsymbol{u}'\boldsymbol{u}'} \right) \right\}. \tag{2.6}$$

Specifically, velocity field data from three adjacent planes are employed to reconstruct the time-averaged pressure distribution using the spectral decomposition-based fast pressure integration algorithm proposed by Wang *et al.* (2017). The divergence of the volumetric velocity fields is corrected using the divergence-free smoothing method developed by Wang *et al.* (2016). It should be noted that the drag evaluation depends on the pressure difference between the exit wake surface Σ_{wake} and the inlet surface Σ_∞. Therefore, the absence of static pressure measurements does not affect the results. The final expression for drag estimation is given by

$$\overline{D} = \int_{\Sigma_{wake}} \overline{d}\, \mathrm{d}S = \int_{\Sigma_{wake}} \rho \overline{u}(U_\infty - \overline{u})\, \mathrm{d}S + \int_{\Sigma_{wake}} (p_\infty - \overline{p})\, \mathrm{d}S + \int_{\Sigma_{wake}} 2\left(\mu \frac{\partial \overline{u}}{\partial x} - \rho \overline{u'u'} \right) \mathrm{d}S, \tag{2.7}$$

where $\overline{d}$ denote drag element. The corresponding force coefficients are computed by

$$\begin{cases} \overline{C}_L = \overline{L} / \left(0.5 \rho U_\infty^2 S\right), & \overline{C}_D = \overline{D} / \left(0.5 \rho U_\infty^2 S\right); \\ \overline{C}_l = \overline{l} / \left(0.5 \rho U_\infty^2 S\right), & \overline{C}_d = \overline{d} / \left(0.5 \rho U_\infty^2 S\right). \end{cases} \tag{2.8}$$

Here, S denotes wing area.

In practice, since the force elements are significant only within a localised subregion of the wake surface, the integration can be restricted to this effective area, as illustrated by the dashed rectangular region in figure 3. It is noted that the flow fields beneath this rectangular region are influenced by the plate support system. Nevertheless, these flow fields are safely excluded from the force estimation, as their contribution to the overall forces is negligible and does not compromise the validity of this study. For ease of description, the streamwise location of the wake surface is denoted as x^*.

3. Dominant flow structures

3.1. *Separation bubble and its associated wake topology*

Figure 4 provides an overview of the dominant flow structures. The first structure discussed herein is the separation bubble, represented by the grey iso-surface of $\overline{u}/U_\infty = 0$. As previously discussed by Zhu *et al.* (2023), the separation bubble emerges at $\alpha = 6°$, featuring a distinct concavity near the midspan. This particular bubble structure is designated as the swallow-tailed structure. With the increase of α, the concavity gradually diminishes and the separation bubble transforms into a conventional single-tailed structure at $\alpha = 10°$. Notably, the swallow-tailed bubble structure is also observed for rectangular plates with $\mathcal{AR}$ ranging from 1.00 to 1.50 at $\alpha = 6°$ (Zhu, Wang & Liu 2024). The reader is referred to Zhu *et al.* (2023, 2024) for the relevant evolution of LEVs over the swallow-tailed separation bubble.

The distribution of time-averaged streamwise vorticity $\overline{\omega}_x$ in the wake exhibits a strong correlation with the separation bubble structure, as illustrated by the colour contours in figure 4. Near the midspan, $\overline{\omega}_x$ is relatively weak at $\alpha = 4°$ (figure 4*a*), whereas large magnitudes of $\overline{\omega}_x$ are observed downstream of the separation bubble for $\alpha = 6°-10°$ (figure 4*b–d*). At these angles of attack, a pair of counter-rotating vortices appears on both lateral sides of the separation bubble, labelled as A in figure 4(*b–d*). Moreover, an additional counter-rotating vortex pair forms when the separation bubble exhibits the swallow-tailed structure, denoted as B in figures 4(*b*) and 4(*c*). This additional vortex

https://doi.org/10.1017/jfm.2026.11791 Published online by Cambridge University Press

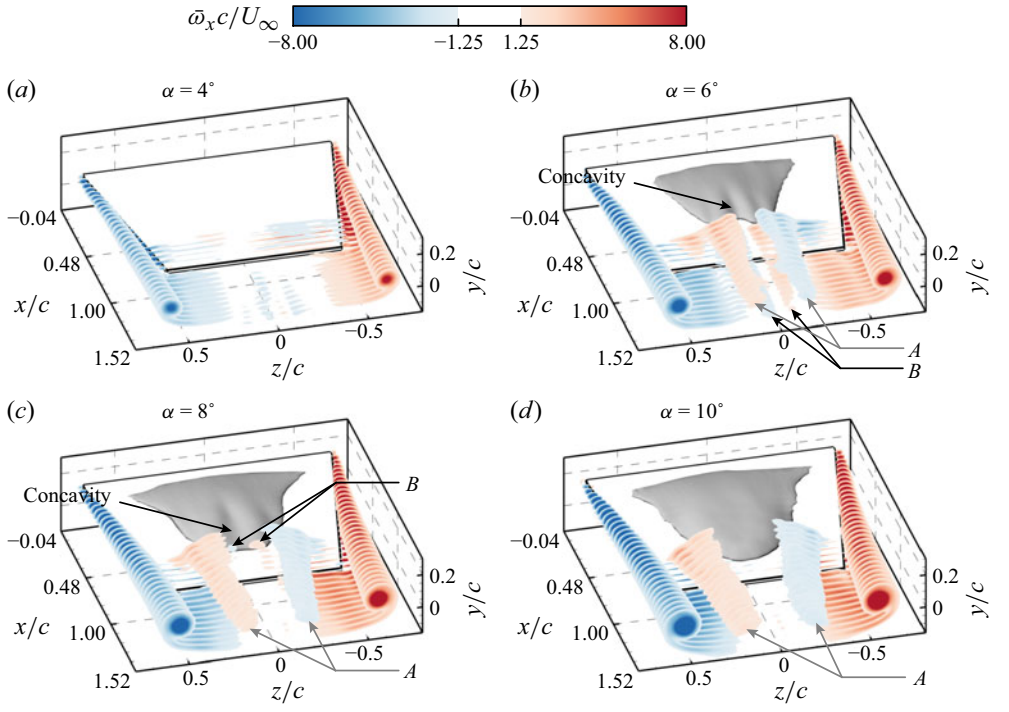


Figure 4. Overview of the flow structures at $\alpha == 4°$–$10°$. Separation bubbles are represented by grey iso-surfaces of $\overline{u}/U_\infty = 0$, while colour contours depict the distribution of time-averaged streamwise vorticity $\overline{\omega}_x$. For enhanced visualisation, contours are blanked over the plate surface upstream of $x/c = 0.74$.

pair persists downstream at $\alpha = 6°$, whereas it becomes indiscernible before reaching the trailing edge at $\alpha = 8°$. This behaviour is consistent with the progressive disappearance of the concavity as α increases. Accordingly, the formation of this additional vortex pair can be attributed to the sufficiently enhanced entrainment in the rear region of the separation bubble during its development into the swallow-tailed structure, as discussed by Zhu *et al.* (2023, 2024). Overall, the streamwise vorticity concentrations (vortex pairs A and B) form a quadrupole pattern at $\alpha = 6°$, originating from the swallow-tailed separation bubble. In contrast, the wake vorticity concentrations at $\alpha = 8°$ and $10°$ constitute a dipole configuration, as only vortex pair A remains in the wake.

To further shed light on the relationship between bubble structures and wake topology, vorticity transport analysis is conducted in the vicinity of the separation bubbles. Specifically, the contributions due to the stretching and tilting terms for the generation of $\overline{\omega}_x$ are evaluated,

$$\begin{cases} \overline{S}_x = & \overline{\omega}_x \dfrac{\partial \overline{u}}{\partial x}; \\ \overline{T}_x = & \overline{\omega}_y \dfrac{\partial \overline{u}}{\partial y} + \overline{\omega}_z \dfrac{\partial \overline{u}}{\partial z}. \end{cases} \tag{3.1}$$

Here, $\overline{S}_x$ and $\overline{T}_x$ denote the time-averaged stretching and tilting terms, respectively. Near the separation bubble, the stretching term is found to be dominant and is further compared between the $\alpha = 6°$ and $10°$ cases, as shown in figure 5. At $\alpha = 6°$, $\overline{S}_x$ is evidently concentrated above the swallow-tailed separation bubble. Particularly, accompanied by the formation of the additional vortex pair B, $\overline{S}_x$ contributes to an increase in local vorticity

https://doi.org/10.1017/jfm.2026.11791 Published online by Cambridge University Press

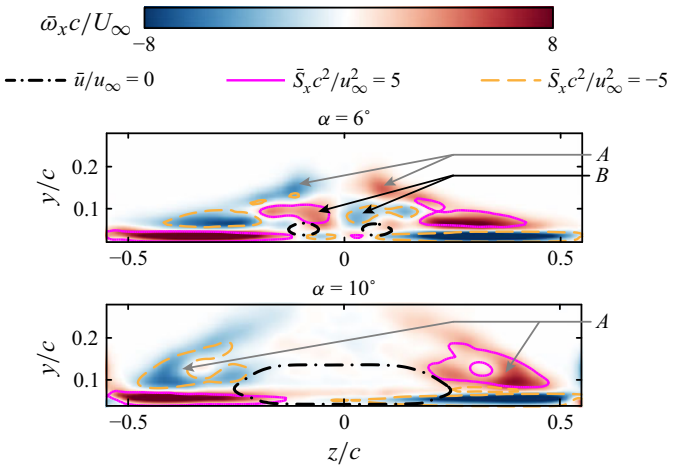


Figure 5. Comparison of the stretching term $\overline{S}_x$ between $\alpha = 6^\circ$ and 10° cases. The sectional shape of the separation bubble is presented using the black dash-dotted lines $\overline{u}/U_\infty = 0$. The vortex pairs A and B are consistent with those in figure 4.

magnitude. In contrast, no obvious $\overline{S}_x$ distribution is captured near the midspan plane at $\alpha = 10^\circ$. This evidence suggests that vortex stretching plays a critical role in the formation of the quadrupole wake topology. Combined with the evolution of LEVs (Zhu *et al.* 2023), the emergence of $\overline{S}_x$ is presumably associated with the LEV transformation from a C-shape to an M-shape structure. However, the detailed physical mechanism still requires further investigation.

3.2. *Characteristics of wingtip vortices*

Another dominant flow structure for the low-$\mathcal{AR}$ plate is the wingtip vortex. As shown in figure 4, a pair of counter-rotating vortices trails from the two side edges of the plate, forming the wingtip vortices. Since the rollup of the wingtip vortices is incomplete in the near field, they exhibit the 'arm-and-fist' pattern, consistent with previous studies (Devenport *et al.* 1996; Skinner, Green & Zare-Behtash 2020).

The characteristics of wingtip vortices are investigated to explore the influence of separation bubble development. The instantaneous locations of the vortex centres $\boldsymbol{x}_c(t)$ are identified from stereo-PIV snapshots via a robust and accurate method based on peak helicity (Skinner *et al.* 2020), given by the following equation:

$$\boldsymbol{x}_c\,(t) = (y_c, z_c) = \arg\max_{y,z} H_x, \quad \text{where} \quad H_x = |u\,(t) - U_\infty| \cdot |\omega_x\,(t)|\,. \tag{3.2}$$

Following Edstrand *et al.* (2016) and Dghim, Ferchichi & Fellouah (2020), the triple decomposition (Hussain & Reynolds 1970) is employed to extract the coherent wandering motion of the wingtip vortex. First, each stereo-PIV snapshot is shifted by $\boldsymbol{x}_c(t)$ into a new reference frame $(\boldsymbol{x} - \boldsymbol{x}_c(t))$, yielding the wandering-corrected velocity field $\hat{\boldsymbol{u}}(\boldsymbol{x} - \boldsymbol{x}_c(t), t)$. The coherent wandering velocity field $\tilde{\boldsymbol{u}}(\boldsymbol{x}, t)$ is then derived as

$$\tilde{\boldsymbol{u}}\,(\boldsymbol{x}, t) = [\boldsymbol{u}\,(\boldsymbol{x}, t) - \overline{\boldsymbol{u}}\,(\boldsymbol{x})] - \left[\hat{\boldsymbol{u}}\,(\boldsymbol{x}, t) - \overline{\hat{\boldsymbol{u}}}\,(\boldsymbol{x})\,\right], \tag{3.3}$$

where the first right-hand term contains the coherent wandering motion and the background turbulence, while the second right-hand term removes the turbulence.

Figure 6 illustrates the core structure of the wingtip vortex with the wandering motion corrected. The wandering-corrected wingtip vortex core structure is analysed through

https://doi.org/10.1017/jfm.2026.11791 Published online by Cambridge University Press

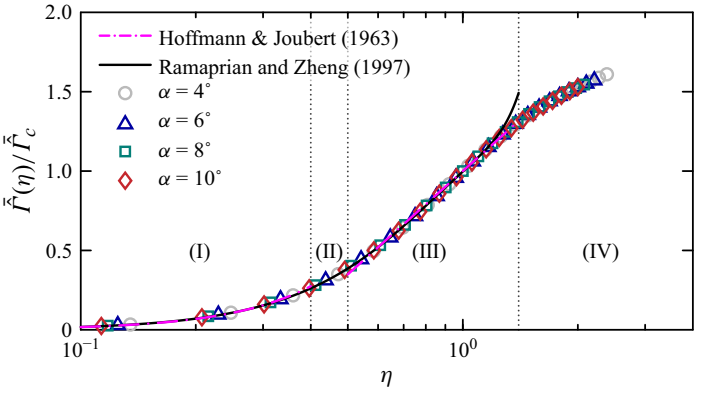


Figure 6. Self-similar wandering-corrected circulation profiles at four angles of attack: (I) inner core region; (II) buffer region; (III) logarithmic region; (IV), outer region.

the radial distribution of the normalised circulation $\overline{\hat{\Gamma}}/\overline{\hat{\Gamma}}_c$, plotted against the similarity variable $\eta = r/\overline{\hat{r}}_c$. Here, circulation $\overline{\hat{\Gamma}}$ is computed via line integration of wandering-corrected tangential velocity along a circular path of radius r centred at the vortex core. The core radius $\overline{\hat{r}}_c$ is defined as the radius where the tangential velocity reaches its maximum and the core circulation is given by $\overline{\hat{\Gamma}}_c = \overline{\hat{\Gamma}}(\overline{\hat{r}}_c)$.

The normalised circulation $\overline{\hat{\Gamma}}/\overline{\hat{\Gamma}}_c$ collapses onto a single curve in figure 6, indicating a self-similar behaviour across different α. To characterise this self-similar behaviour, two empirical curve-fitting models are applied. First, for the inner region ($\eta < 1.4$), Hoffmann & Joubert (1963) proposed the following model:

$$\begin{cases} \overline{\hat{\Gamma}}(\eta)/\overline{\hat{\Gamma}}_c = A\eta^2 & \text{for } \eta < 0.4, \\ \overline{\hat{\Gamma}}(\eta)/\overline{\hat{\Gamma}}_c = 1 + B\log(\eta) & \text{for } 0.5 < \eta < 1.4. \end{cases} \tag{3.4}$$

In the present study, the curve-fitting constants A and B are determined as 1.717 and 2.163, respectively. Second, Ramaprian & Zheng (1997) demonstrated that $\overline{\hat{\Gamma}}/\overline{\hat{\Gamma}}_c$ follows a sixth-order polynomial for $\eta < 1.2$, given by

$$\overline{\hat{\Gamma}}(\eta)/\overline{\hat{\Gamma}}_c = a_0\eta^2 + a_1\eta^4 + a_2\eta^6. \tag{3.5}$$

Herein, a_0, a_1 and a_2 take values of 1.799, −1.085 and 0.284, respectively. As shown in figure 6, the normalised circulation profiles are in excellent agreement with these empirical fitting curves. Furthermore, these five curve-fitting constants agree well with the published results (Birch *et al.* 2004; Gerontakos & Lee 2006). These results suggest that the core structure of the wingtip vortices remains unaffected by separation bubble development across all tested angles of attack.

To gain insight into the coupling between wingtip vortices and separation bubbles, POD is applied to the coherent wandering velocity fields $\tilde{\boldsymbol{u}}(\boldsymbol{x}, t)$ at each cross-section y–z plane (Edstrand *et al.* 2016; Dghim *et al.* 2020), expressed as

$$\tilde{\boldsymbol{u}}(\boldsymbol{x}, t) = \sum_{k}^{N} a_k \tilde{\boldsymbol{u}}^{\phi(k)}. \tag{3.6}$$

https://doi.org/10.1017/jfm.2026.11791 Published online by Cambridge University Press

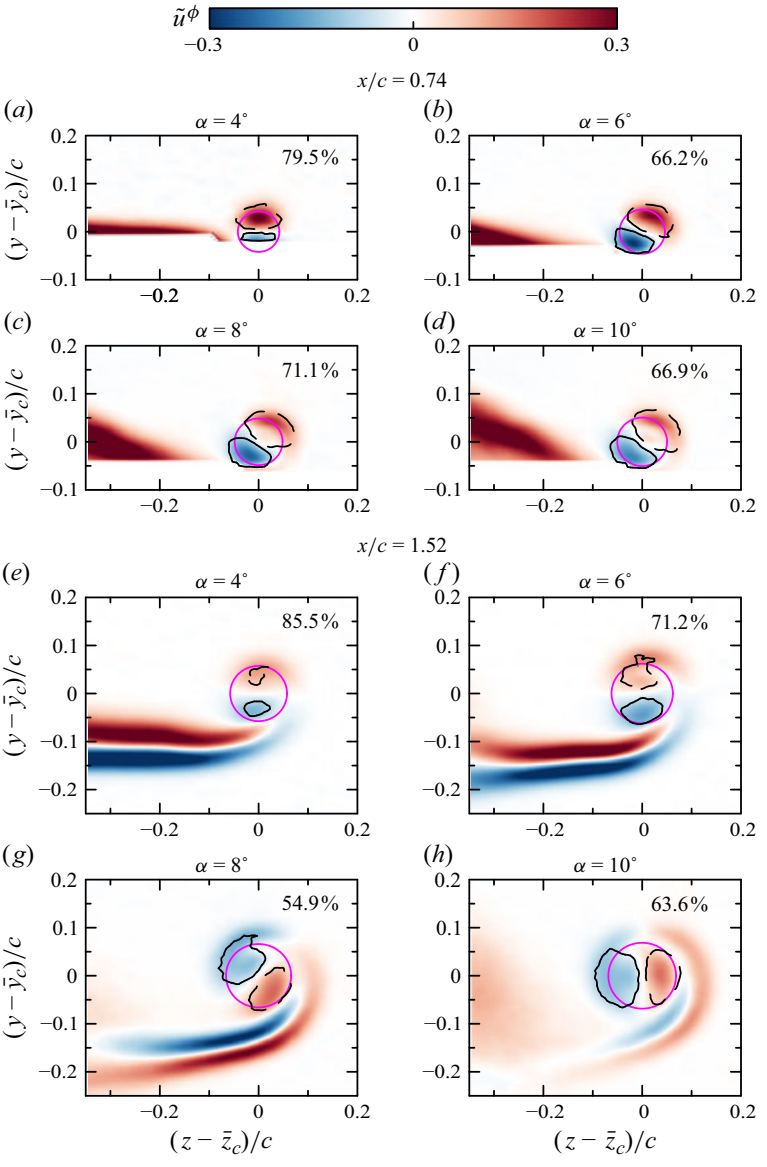


Figure 7. Streamwise velocity contours of the leading POD mode for the wingtip vortex with positive $\overline{\omega}_x$. Magenta circles denote the locations of the wingtip vortex cores. Solid and dashed black contour lines represent $\tilde{\omega}_x^{\phi(1)} = 0.0075$ and -0.0075 within each circle, respectively. The percentage in the upper right corner of each panel represents the energy ratio of the corresponding POD mode to the total fluctuation energy.

Here, a_k is the time coefficient of the kth mode $\tilde{\boldsymbol{u}}^{\phi(k)}$ and N denotes the total number of modes. Figure 7 presents the streamwise velocity component of the leading POD mode $\tilde{u}^{\phi(1)}$ at $x/c = 0.74$ and 1.52. This dominant POD mode accounts for more than half of the total fluctuation energy of the wingtip vortex at a given plane, as quantified by the percentage values in each panel of figure 7. The cross-sectional positions of the wingtip vortex cores are indicated by magenta circles, with radii corresponding to the local vortex core radius $\hat{r}_c$. Owing to the plate symmetry, this study is restricted to the wingtip

https://doi.org/10.1017/jfm.2026.11791 Published online by Cambridge University Press

vortices with positive streamwise vorticity $\overline{\omega}_x$. Within each magenta circle, two regions of oppositely signed $\tilde{u}^{\phi(1)}$ are clearly observed. The formation of this velocity distribution is consistent with prior studies and is associated with the helical displacement of the wingtip vortices (Edstrand *et al.* 2016; Dghim *et al.* 2021).

To illustrate the implications of the $\tilde{u}^{\phi(1)}$ distribution on the wandering motion of the wingtip vortex, the corresponding modal streamwise vorticity $\tilde{\omega}_x^{\phi(1)}$ within each magenta circle is shown in figure 7. The distribution of $\tilde{\omega}_x^{\phi(1)}$ is represented by solid and dashed black contour lines, corresponding to $\tilde{\omega}^{\phi(1)} = 0.0075$ and -0.0075, respectively. For each vortex core, regions of oppositely signed $\tilde{\omega}_x^{\phi(1)}$ are symmetrically positioned on either side. When the time coefficient a_1 assumes a positive value, vorticity intensifies on the side with positive $\tilde{\omega}_x^{\phi(1)}$ and weakens on the side with negative $\tilde{\omega}_x^{\phi(1)}$, given that the wingtip vortex has positive $\overline{\omega}_x$ as described earlier. As a result, the vortex cores undergo systematic displacement along the axis connecting these two regions, wandering from the negative to the positive $\tilde{\omega}_x^{\phi(1)}$ side.

Notably, on the left side of the vortex cores (i.e. $(z - \overline{z}_c)/c < 0$), $\tilde{u}^{\phi(1)}$ exhibits distinct behaviour depending on separation bubble development. As shown in figure 7(*a*), $\tilde{u}^{\phi(1)}$ is relatively uniformly along the spanwise direction for $\alpha = 4°$. In the absence of a separation bubble, this $\tilde{u}^{\phi(1)}$ distribution is attributed to attached boundary layer instability. Correspondingly, the wingtip vortex displays a vertical wandering tendency, as inferred from the $\tilde{\omega}_x^{\phi(1)}$ regions within the magenta circle. In contrast, at higher angles of attack, $\tilde{u}^{\phi(1)}$ becomes concentrated in the region $(z - \overline{z}_c)/c < -0.2$ and the wingtip vortices exhibit a spanwise wandering tendency. Specifically, when a_1 is positive, the localised positive $\tilde{u}^{\phi(1)}$ on the left side of each vortex core indicates the contraction of the separation bubble. This bubble contraction is accompanied by the leftward wandering of wingtip vortices.

Similar $\tilde{u}^{\phi(1)}$ behaviour is observed in the wake. For $\alpha \leqslant 6°$, the $\tilde{u}^{\phi(1)}$ distribution outside the wingtip vortex cores originates from the wake shear layers and the wingtip vortices display a tendency of vertical wandering (figures 7*e* and 7*f*). As α increases to 10°, a concentrated $\tilde{u}^{\phi(1)}$ region induced by the separation bubble appears at the left side of the wingtip vortex core, accompanied by a pronounced spanwise wandering tendency of the wingtip vortex (figure 7*h*). In summary, the results demonstrate that the oscillation of separation bubbles strengthens with increasing α and promotes the spanwise wandering of the wingtip vortices.

4. Linking flow structures and aerodynamic forces

In this section, the overall aerodynamic performance of the trapezoidal plate is first evaluated. Subsequently, the distribution of force elements is presented to shed light on how flow structures influence aerodynamic performance.

Figure 8 illustrates the overall aerodynamic performance of the trapezoidal plate. The uncertainties in velocity statistics are calculated following Sciacchitano & Wieneke (2016) and the pressure uncertainty is then estimated using the sequential perturbation method from Moffat (1988). As shown in figure 8(*a*), the time-averaged lift coefficient $\overline{C}_L$ increases with increasing α and is independent of the streamwise position x^* of the wake plane Σ_{wake}. An increasing trend is also observed for the time-averaged drag coefficient $\overline{C}_D$ in figure 8(*b*). Despite a slight increase for $x^* < 1.24$, $\overline{C}_D$ remains nearly constant for each α case. Due to the small magnitude of $\overline{C}_D$, the corresponding uncertainty in drag estimation is more prominent than that of lift. Furthermore, figure 8(*c*) shows the variation of the time-averaged lift-to-drag ratio $\overline{C}_L/\overline{C}_D$ against α. Notably, $\overline{C}_L/\overline{C}_D$ reaches its peak

https://doi.org/10.1017/jfm.2026.11791 Published online by Cambridge University Press

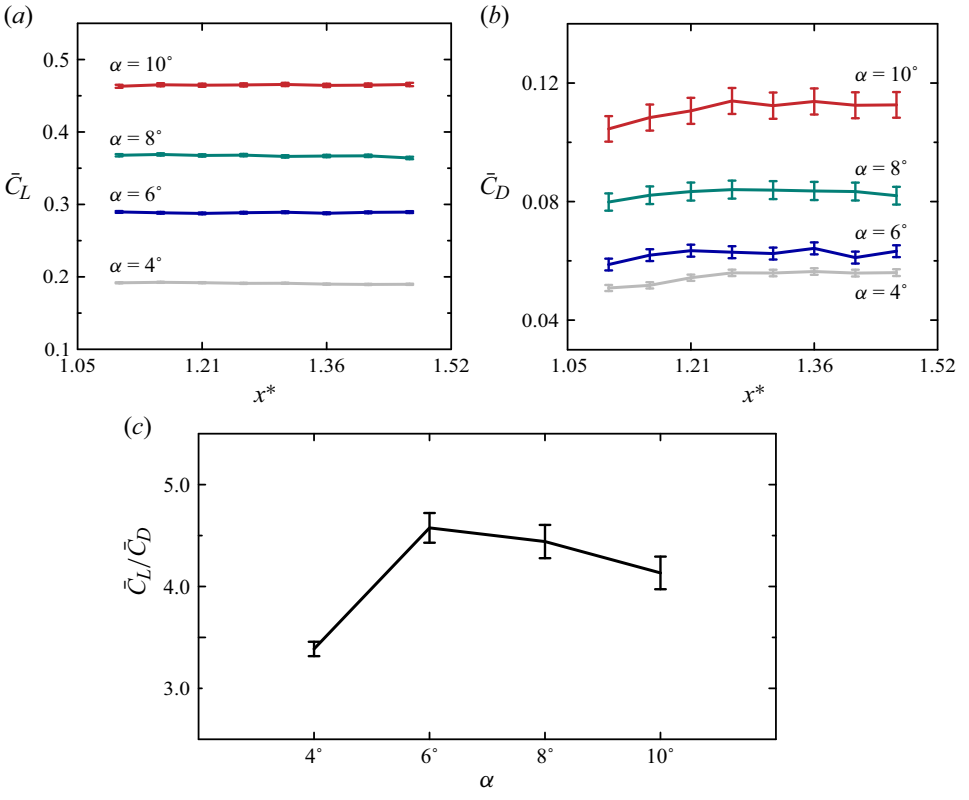


Figure 8. Variation of (*a*) time-averaged lift and (*b*) drag coefficients versus streamwise position x^* of the wake plane Σ_{wake}. (*c*) Variation of lift-to-drag ratio $\overline{C}_L/\overline{C}_D$ versus α for the Σ_{wake} position $x^* = 1.49$.

at $\alpha = 6°$. This implies that the maximum $\overline{C}_L/\overline{C}_D$ is associated with the formation of the swallow-tailed separation bubble at this angle of attack.

To clarify the implications of bubble structures on aerodynamic forces, figure 9 compares the lift and drag elements corresponding to $x^* = 1.52$. The solid and dashed lines correspond to $\overline{\omega}_x c/U_\infty = 1.25$ and -1.25, respectively. Specifically, the wingtip vortices are depicted by grey lines, while the multipoles induced by separation bubbles are represented by black lines. According to figure 9(*a*), the time-averaged lift element $\overline{C}_l$ is predominantly distributed in the tip vortex regions across all four α. In contrast, the distribution of the time-averaged drag element $\overline{C}_d$ in figure 9(*b*) shows that drag originates from both the tip vortex regions and the regions surrounding the multipoles. Despite the variation of α, the contribution of tip vortex regions to the total drag is maintained below 35 %. These results demonstrate that the formation and structural evolution of the separation bubble exert a pronounced influence on drag.

Given the critical role of velocity deficit in drag generation, the wake velocity deficit associated with the separation bubble is further investigated. In figure 9(*b*), the blue dash-dotted lines of $(\overline{u} - U_\infty)/U_\infty = -0.35$ delineate regions of high-magnitude velocity deficit. At $\alpha = 4°$, the velocity deficit is uniformly distributed along the spanwise direction with no separation bubble present. For $\alpha \geqslant 6°$, the high-magnitude velocity deficit becomes concentrated near the midspan and its extent expands with increasing α. Notably, at $\alpha = 8°$ and 10°, the spanwise spacing of the $\overline{\omega}_x$ dipoles is approximately equal to the spanwise size of the high-magnitude velocity deficit region. In contrast, at $\alpha = 6°$, a

https://doi.org/10.1017/jfm.2026.11791 Published online by Cambridge University Press

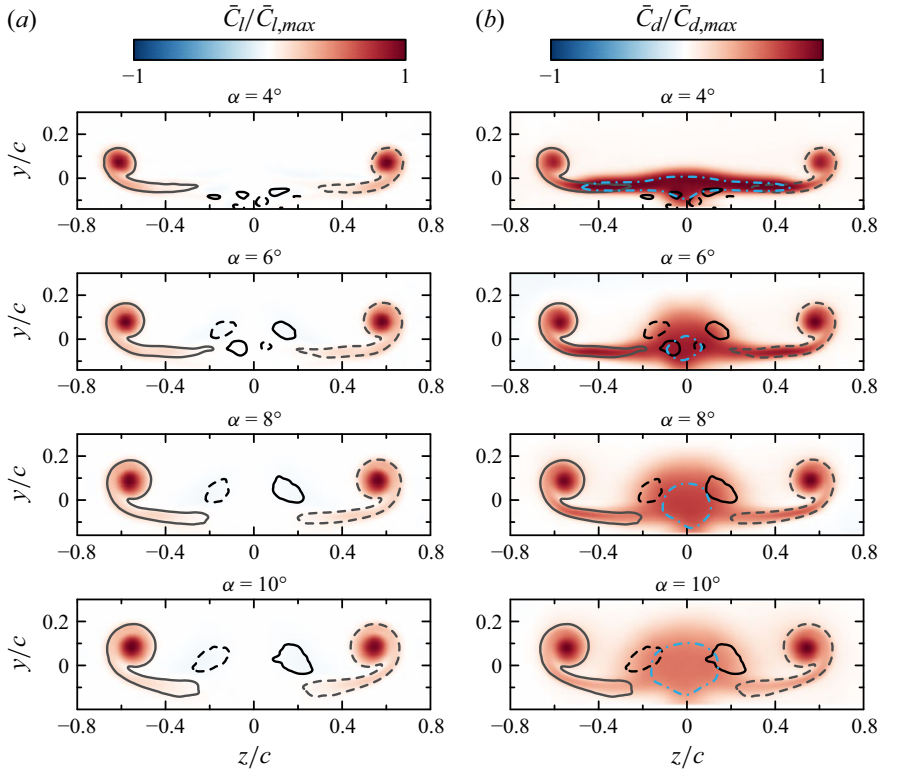


Figure 9. Distribution of the (*a*) lift and (*b*) drag elements corresponding to $x^* = 1.49$. Solid and dashed lines correspond to $\overline{\omega}_x c/U_\infty = 1.25$ and -1.25, respectively, denoting the wingtip vortices (grey lines) and multipoles (black lines). The blue dash-dotted lines of $(\overline{u} - U_\infty)/U_\infty = -0.35$ depict the regions with high-magnitude velocity deficit.

significant contraction in the spanwise extent of the velocity deficit region is observed, coinciding with the emergence of the additional counter-rotating vortex pair. In other words, the formation of the $\overline{\omega}_x$ quadrupole in the wake contributes to the reduction in velocity deficit. Therefore, the swallow-tailed structure facilitates drag reduction, resulting in the maximum lift-to-drag ratio at $\alpha = 6°$.

5. Concluding remarks

An experimental investigation on flow structures and aerodynamic characteristics of a low-$\mathcal{AR}$ trapezoidal plate at a low Reynolds number of $Re_c = 5800$ is conducted. The angle of attack ranges from 4° to 10°. The volumetric flow fields are measured with stereo-PIV and the aerodynamic forces are subsequently obtained using the wake-integral approach. It is revealed that the development of separation bubbles has a significant role in wake topology and aerodynamic performance.

For the swallow-tailed separation bubble exhibiting distinct concavity, the associated time-averaged wake topology takes a quadrupole configuration, consisting of four streamwise vorticity concentrations. The formation of the counter-rotating vortex pair on both lateral sides of the swallow-tailed bubble is analogous to that observed in conventional single-tailed bubbles, whereas the emergence of the additional counter-rotating vortex pair is attributed to enhanced entrainment in the rear region of the swallow-tailed bubble. Furthermore, oscillations of the separation bubbles prompt the

https://doi.org/10.1017/jfm.2026.11791 Published online by Cambridge University Press

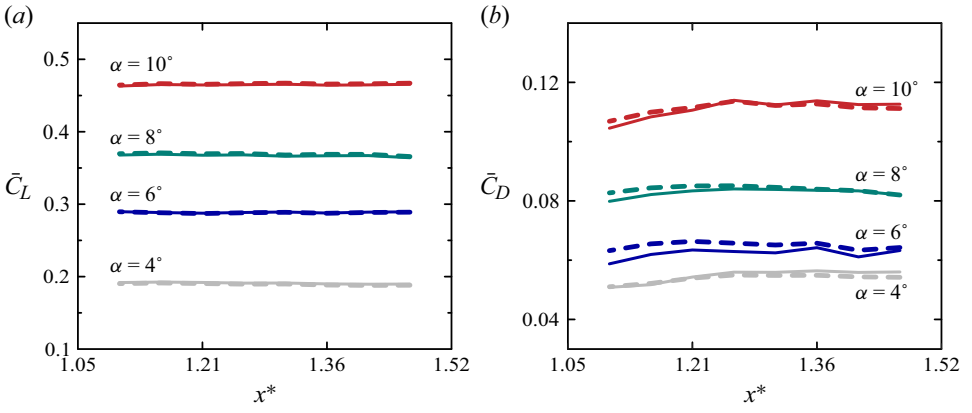


Figure 10. Effects of integration window size on (*a*) lift and (*b*) drag estimations. The dashed and solid lines correspond to the results from the narrowed and original integration windows, respectively.

wandering motion of the wingtip vortices, with this effect intensifying as α increases. Notably, the core structure of the wingtip vortices remains unaltered.

The wake-integral aerodynamic force analysis indicates that lift depends primarily on the wingtip vortex region, while drag is associated with both the wingtip vortex and the wake deficit induced by the separation bubble. Both lift and drag increase with increasing α. Notably, the lift-to-drag ratio of the plate reaches the maximum value when the separation bubble features the swallow-tailed structure at $\alpha = 6^\circ$. This is attributed to the formation of the quadrupole wake topology. It is the additional vortex pair that restricts the expansion of the high-magnitude velocity deficit region, thereby contributing to drag reduction.

In summary, the implications of the swallow-tailed separation bubble structure on aerodynamic forces is now brought to light, advancing the vortex dynamics analysis presented in our previous works (Zhu *et al.* 2023, 2024). In addition to the trapezoidal plate investigated herein, swallow-tailed separation bubbles also emerge on rectangular plates with an $\mathcal{AR}$ ranging from 1.00 to 1.50. Accordingly, the implications of the swallow-tailed bubble structure are considered applicable to low-$\mathcal{AR}$ plates at comparable Reynolds numbers. Furthermore, these findings provide practical guidance for engineering applications by demonstrating the effectiveness of physics-based flow control techniques as discussed by Zhu *et al.* (2023).

Acknowledgements. We thank the anonymous referees for their constructive comments in improving this manuscript.

Funding. This work is supported by the National Natural Science Foundation of China (Grant No. 11721202).

Declaration of interests. The authors report no conflict of interest.

Appendix A. Validation of the estimated aerodynamic forces

Validation is performed from two perspectives: evaluating the sensitivity of aerodynamic forces to the integration window size; and comparing the estimated forces with published data under comparable flow conditions.

First, the upper and lateral boundaries of the integration window are each contracted inward by $0.1c$, and aerodynamic forces are recalculated within this reduced domain. Figure 10 compares the aerodynamic coefficients obtained from the original and narrowed

https://doi.org/10.1017/jfm.2026.11791 Published online by Cambridge University Press

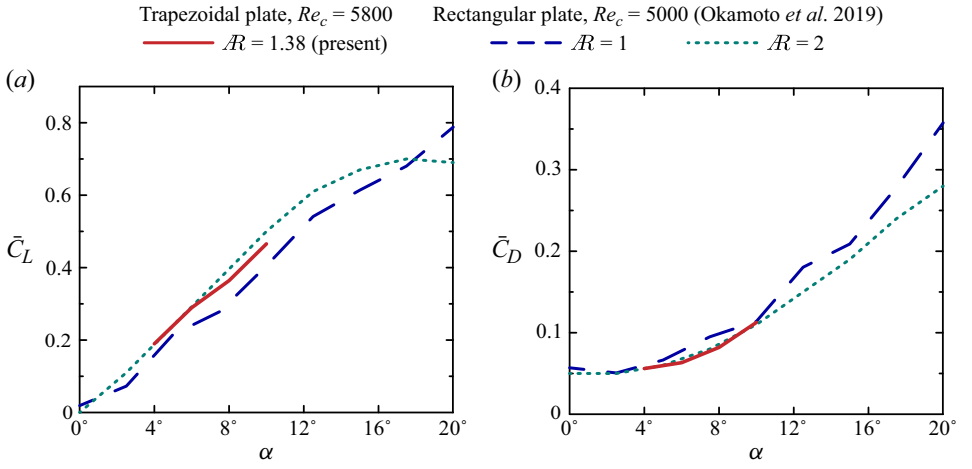


Figure 11. Variation of time-averaged (*a*) lift and (*b*) drag coefficients versus α for $x^* = 1.49$. The red solid lines denote the results from the present study, while the blue dashed and green dotted lines correspond to the measured force coefficients reported by Okamoto *et al.* (2019).

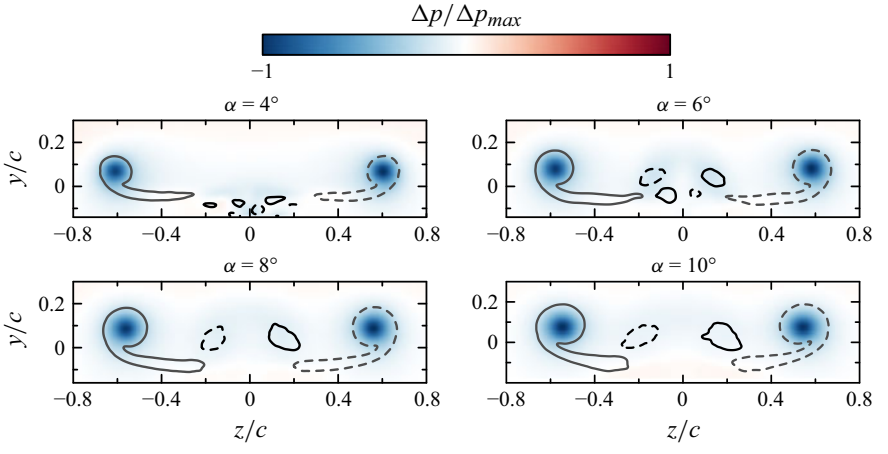


Figure 12. Distribution of pressure differences $\Delta p = \overline{p} - p_\infty$ at $x^* = 1.49$. Solid and dashed lines correspond to $\overline{\omega}_x c/U_\infty = 1.25$ and -1.25, respectively.

integration windows as a function of x^*. It is evident that reducing the window size exerts only a minor influence on the calculated aerodynamic forces.

Second, a comparison with the dataset from Okamoto *et al.* (2019) under comparable flow conditions is presented in figure 11. The time-averaged aerodynamic coefficients estimated in the present work agree with the measurements of Okamoto *et al.* (2019), thereby validating the accuracy and feasibility of the wake-integral force estimation method adopted in this study.

Appendix B. Distribution of the pressure differences

Figure 12 presents the distribution of pressure difference $\Delta p = \overline{p} - p_\infty$ at $x^* = 1.49$ obtained using (2.6). Low-pressure regions are mainly concentrated in the vicinity of the

https://doi.org/10.1017/jfm.2026.11791 Published online by Cambridge University Press

wingtip vortices, which is consistent with the observations reported by Roeland & Robert (2016).

References

Baker, N.T., Diaz, D., Bailly, D., David, L. & Monnier, J.-C. 2019 Mechanical vs. phenomenological formulations to determine mean aerodynamic drag from stereo-PIV wake measurements. *Exp. Fluids* **60**, 167.

Birch, D., Lee, T., Mokhtarian, F. & Kafyeke, F. 2004 Structure and induced drag of a tip vortex. *J. Aircraft* **41**, 1138–1145.

Devenport, W.J., Rife, M.C., Liapis, S.I. & Follin, G.J. 1996 The structure and development of a wing-tip vortex. *J. Fluid Mech.* **312**, 67–106.

Dghim, M., Ben Miloud, K., Ferchichi, M. & Fellouah, H. 2021 Meandering of a wing-tip vortex in a grid-generated turbulent flow. *Phys. Fluids* **33**, 115131.

Dghim, M., Ferchichi, M. & Fellouah, H. 2020 On the effect of active flow control on the meandering of a wing-tip vortex. *J. Fluid Mech.* **896**, A30.

Dong, L., Choi, K.-S. & Mao, X.R. 2020 Interplay of the leading-edge vortex and the tip vortex of a low-aspect-ratio thin wing. *Exp. Fluids* **61**, 200.

Edstrand, A.M., Davis, T.B., Schmid, P.J., Taira, K. & Cattafesta, L.N. 2016 On the mechanism of trailing vortex wandering. *J. Fluid Mech.* **801**, R1.

Garmann, D.J. & Visbal, M.R. 2017 Investigation of the unsteady tip vortex structure on a NACA0012 wing at fixed incidence. *AIAA Paper* 2017-1002. AIAA.

Gerontakos, P. & Lee, T. 2006 Near-field tip vortex behind a swept wing model. *Exp. Fluids* **40**, 141–155.

Hoffmann, E.R. & Joubert, P.N. 1963 Turbulent line vortices. *J. Fluid Mech.* **16**, 395–411.

Hu, Y. & Wang, J.J. 2011 Dual leading-edge vortex structure for flow over a simplified butterfly model. *Exp. Fluids* **50**, 1285–1292.

Hussain, A.K.M.F. & Reynolds, W.C. 1970 The mechanics of an organized wave in turbulent shear flow. *J. Fluid Mech.* **41**, 241–258.

Mendez, M.A., Raiola, M., Masullo, A., Discetti, S., Ianiro, A., Theunissen, R. & Buchlin, J.-M. 2017 POD-based background removal for particle image velocimetry. *Exp. Therm. Fluid Sci.* **80**, 181–192.

Moffat, R.J. 1988 Describing the uncertainties in experimental results. *Exp. Therm. Fluid Sci.* **1**, 3–17.

Mueller, T.J. 1999 Aerodynamic measurements at low Reynolds numbers for fixed wing micro-air vehicles. In *RTO AVT/VKI Special Course on Development and Operation of UAVs for Military and Civil Applications*.

Navrose, B., V, & Jacquin, L. 2019 Transient growth in the near wake region of the flow past a finite span wing. *J. Fluid Mech.* **866**, 399–430.

Okamoto, M., Sasaki, D., Kamikubo, M. & Fujii, R. 2019 Disappearance of vortex lift in low-aspect-ratio wings at very-low Reynolds numbers. *Trans. Japan Soc. Aeronaut. Space Sci.* **62**, 310–317.

Ortega Ancel, A., Eastwood, R., Vogt, D., Ithier, C., Smith, M., Wood, R. & Kovač, M. 2017 Aerodynamic evaluation of wing shape and wing orientation in four butterfly species using numerical simulations and a low-speed wind tunnel, and its implications for the design of flying micro-robots. *Interface Focus* **7**, 20160087.

Pan, C., Xue, D., Xu, Y., Wang, J.J. & Wei, R.J. 2015 Evaluating the accuracy performance of Lucas–Kanade algorithm in the circumstance of PIV application. *Sci. China Phys. Mech. Astron.* **58**, 104704.

Pandi, J.S.S. & Mittal, S. 2023 Streamwise vortices, cellular shedding and force coefficients on finite wing at low Reynolds number. *J. Fluid Mech.* **958**, A10.

Ramaprian, B.R. & Zheng, Y.X. 1997 Measurements in rollup region of the tip vortex from a rectangular wing. *AIAA J.* **35**, 1837–1843.

Ribeiro, J.H.M., Neal, J., Burtsev, A., Amitay, M., Theofilis, V. & Taira, K. 2023*a* L*a*minar post-stall wakes of tapered swept wings. *J. Fluid Mech.* **976**, A6.

Ribeiro, J.H.M., Yeh, C.-A. & Taira, K. 2023*b* Triglo*b*al resolvent analysis of swept-wing wakes. *J. Fluid Mech.* **954**, A42.

Roeland, D.K. & Robert, B. 2016 Towards instantaneous lift and drag from stereo-PIV wake measurements. In *Proceedings of the 18th International Symposium on Application of Laser and Imaging Techniques to Fluid Mechanics*.

Scherl, I., Strom, B., Shang, J.K., Williams, O., Polagye, B.L. & Brunton, S.L. 2020 Robust principal component analysis for modal decomposition of corrupt fluid flows. *Phys. Rev. Fluids* **5**, 054401.

Sciacchitano, A. & Wieneke, B. 2016 PIV uncertainty propagation. *Meas. Sci. Technol.* **27**, 084006.

https://doi.org/10.1017/jfm.2026.11791 Published online by Cambridge University Press

SIROVICH, L. 1987 Turbulence and the dynamics of coherent structures. III. Dynamics and scaling. *Q. Appl. Math.* **45**, 583–590.

SKINNER, S.N., GREEN, R.B. & ZARE-BEHTASH, H. 2020 Wingtip vortex structure in the near-field of swept-tapered wings. *Phys. Fluids* **32**, 095102.

SOLOFF, S.M., ADRIAN, R.J. & LIU, Z.-C. 1997 Distortion compensation for generalized stereoscopic particle image velocimetry. *Meas. Sci. Technol.* **8**, 1441–1454.

TONG, W.W., WANG, S.Z. & YANG, Y. 2022 Estimating forces from cross-sectional data in the wake of flows past a plate using theoretical and data-driven models. *Phys. Fluids* **34**, 111905.

TOPPINGS, C.E. & YARUSEVYCH, S. 2021 Structure and dynamics of a laminar separation bubble near a wingtip. *J. Fluid Mech.* **929**, A39.

VAN DAM, C.P. 1999 Recent experience with different methods of drag prediction. *Prog. Aerosp. Sci.* **35**, 751–798.

VAN DOORNE, C.W.H. & WESTERWEEL, J. 2007 Measurement of laminar, transitional and turbulent pipe flow using Stereoscopic-PIV. *Exp. Fluids* **42**, 259–279.

WANG, C.Y., GAO, Q., WANG, H.P., WEI, R.J., LI, T. & WANG, J.J. 2016 Divergence-free smoothing for volumetric PIV data. *Exp. Fluids* **57**, 15.

WANG, C.Y., GAO, Q., WEI, R.J., LI, T. & WANG, J.J. 2017 Spectral decomposition-based fast pressure integration algorithm. *Exp. Fluids* **58**, 84.

WANG, S.Z., HE, G.W. & LIU, T.S. 2019 Estimating lift from wake velocity data in flapping flight. *J. Fluid Mech.* **868**, 501–537.

WIENEKE, B. 2005 Stereo-PIV using self-calibration on particle images. *Exp. Fluids* **39**, 267–280.

WINSLOW, J., OTSUKA, H., GOVINDARAJAN, B. & CHOPRA, I. 2018 Basic understanding of airfoil characteristics at low Reynolds numbers (10^4–10^5). *J. Aircraft* **55**, 1050–1061.

ZHANG, K., HAYOSTEK, S., AMITAY, M., HE, W., THEOFILIS, V. & TAIRA, K. 2020 On the formation of three-dimensional separated flows over wings under tip effects. *J. Fluid Mech.* **895**, A9.

ZHU, Y.C., LIU, J.X. & WANG, J.J. 2025 Reversal of nonlinear energy transfer direction in flows over low-aspect-ratio plates. *J. Fluid Mech.* **1010**, A1.

ZHU, Y.C., QU, Y., WANG, J.J. & MA, B.F. 2020 Near-wall topological patterns and flow structures over a simplified Danaus plexippus model. *Chin. J. Aeronaut.* **33**, 2527–2534.

ZHU, Y.C., WANG, J.J. & LIU, J.X. 2024 Tip effects on three-dimensional flow structures over low-aspect-ratio plates: mechanisms of spanwise fluid transport. *J. Fluid Mech.* **983**, A35.

ZHU, Y.C., WANG, J.J., XU, Y., QU, Y. & LONG, Y.G. 2023 Swallow-tailed separation bubble on a low-aspect-ratio trapezoidal plate: effects of near-wall spanwise flow. *J. Fluid Mech.* **965**, A12.

https://doi.org/10.1017/jfm.2026.11791 Published online by Cambridge University Press